Available online at website: https://journal.bcrec.id/index.php/bcrec

Bulletin of Chemical Reaction Engineering & Catalysis, 19 (2) 2024, 285-299

Research Article

Designing A Visible Light Driven TiO_2-Based Photocatalyst by Doping and Co-Doping with Niobium (Nb) and Boron (B)

Jia-Zheng Yeoh[1], Phei-Lim Chan[1], Swee-Yong Pung[1], Sivakumar Ramakrishnan[1,*], Collin G. Joseph[2], Chia-Yun Chen[3]

[1]*School of Materials and Mineral Resources Engineering, Engineering Campus, Universiti Sains Malaysia, Penang, Malaysia.*
[2]*Faculty of Science and Natural Resources / Industrial Chemistry Programme, University Malaysia Sabah, Sabah, Malaysia.*
[3]*Department of Materials Science and Engineering, National Cheng Kung University, Tainan City, Taiwan.*

Received: 5th March 2024; Revised: 13th June 2024; Accepted: 14th June 2024
Available online: 16th June 2024; Published regularly: August 2024

Abstract

Water pollution has emerged as a significant worldwide issue, with organic pollutants being a key contributor. Titanium dioxide (TiO_2) has demonstrated promising photocatalytic performance in removing organic pollutants under ultraviolet (UV) irradiation. However, the wide band gap (3.2 eV) of TiO_2 results in low absorption capacity of visible light, hindering its overall efficiency in degrading organic pollutants. To address the limitation, this research aimed to synthesize visible light-driven TiO_2 photocatalyst with different polymorphs (anatase and rutile) and investigate the effect of various doping combination (Nb, B and Nb,B) and concentrations (0.25, 0.50, 0.75 and 1.00 mol%) on the photodegradation efficiency towards methylene blue (MB) dye solution. Anatase phase was obtained when TiO_2-based nanopowders were calcined at 400 °C, while the rutile phase was formed at 900 °C based on XRD analyses. Additionally, the morphology analyses revealed that the particle size of anatase is much smaller than that of rutile. The presence of dopants further reduced the particle size of both anatase and rutile phases. Based on UV-Vis absorbance spectra analyses, the anatase Nb,B-TiO_2 with 0.50 mol% of dopant concentration exhibited the best photocatalytic performance towards MB. Moreover, the anatse phase of 0.50 mol% Nb,B-TiO_2 showed the narrowest band gap of 2.74 eV compared to the TiO_2 (3.4 eV), representing a reduction of 19.41 %, according to UV-Vis analyses. These outcomes suggest the potential application of anatase phase of 0.50 mol% Nb,B-TiO_2 in treating organic pollutants in wastewater under visible light conditions in future.

Keywords: TiO_2; anatase; doping; visible light-driven; band gap energy reduction

How to Cite: J.Z. Yeoh, P.L. Chan, S.Y. Pung, S. Ramakrishnan, C.G. Joseph, C.Y. Chen (2024). Designing A Visible Light Driven TiO_2-Based Photocatalyst by Doping and Co-Doping with Niobium (Nb) and Boron (B). *Bulletin of Chemical Reaction Engineering & Catalysis*, 19 (2), 285-299 (doi: 10.9767/bcrec.20137)

Permalink/DOI: https://doi.org/10.9767/bcrec.20137

1. Introduction

Growing populations and economies are significantly increasing the demand for urbanization and industrialization. Particularly, industrialization has led to severe global challenges, including water pollution, energy crises and public health issues [1,2]. One major contributor to water pollution is the release of synthetic dyes. These organic pollutants are particularly difficult to remove from water, worsening issues with water pollution and the unavailability of clean drinking water [3-7]. Despite these issues, synthetic dyes are extensively used in various industries such as textiles, food, printing, and paper to meet human necessaries [8-10].

Among synthetic dyes, methylene blue (MB) has drawn significant attention as a model organic pollutant for photodegradation studies. MB is a cationic dye with highly water-soluble

---

* Corresponding Author.
Email: srsivakumar@usm.my (S. Ramakrishnan);
Telp: +60 12-4393120, Fax: +60 4-5996110

properties, forming a stable solution with water at room temperature [2,8]. As a result, MB is commonly used as colorant for plastic, cotton, wool, leather, and silk [11-13]. Additionally, MB solution is reportedly toxic, carcinogenic, and non-biodegradable, endangering human health and negatively impacting the environment [11,12]. Therefore, this research selects MB as the model organic pollutant for photodegradation studies.

Various treatment techniques have been reported and established for wastewater remediation, including sedimentation [14,15], filtration [16,17], biofilms [18,19] and activated sludge [20,21]. However, these existing techniques encounter challenges in completely removing non-biodegradable pollutants due to constraints such as high chemical and energy consumption, prolonged reaction time, high operating costs, sludge generation and toxic gas release [22,23]. Therefore, semiconductor-based photocatalysts have drawn significant attention for wastewater remediation due to their capability to efficiently remove pollutants, transforming them into harmless by-products under light irradiation [24-27].

Titanium dioxide (TiO_2) is a promising material for semiconductor-based photocatalysts due to its excellent optical properties, affordability, high photocatalytic activity, chemical stability, and non-toxicity [25-27]. TiO_2 has several polymorphs, including brookite, anatase, and rutile, with rutile being the most stable in the crystal phase [25,28,29]. This stability is attributed to the higher surface energy of rutile compared to anatase, which causes the particles to agglomerate, resulting in larger sizes and smaller specific surface areas [30-32]. However, the application of anatase or rutile phases in photocatalysis remains debated [33, 34]. Both bare TiO_2 phases are generally restricted in the photocatalytic performance, as they are primarily activated under UV light due to their wide band gap (3.2 eV) [35-37]. This requires a substantial energy supply to continuously generate the needed light for such treatment purposes. Additionally, solar irradiation contains less than 5% of UV light, which is insufficient to activate bare TiO_2 for effective photodegradation. Furthermore, bare TiO_2 shows a high tendency for recombination of photo-generated electron-hole pairs, reducing the overall efficiency of the photocatalyst [35-37]. To address these limitations, various studies have focused on enhancing the photocatalytic performance of TiO_2 through metal or non-metal doping [25-27]. Doping improves the mobility of photo-generated carriers by effectively separating electrons and holes with a moderate amount of dopants. This reduces particle agglomeration, increases the surface area of the photocatalyst, and enhances its overall efficiency.

In this research, niobium (Nb) and boron (B) were selected as dopants to modify TiO_2 through the sol-gel technique. Niobium is an *n*-type dopant that provides excess electrons to the TiO_2 lattice, generating negative charge carriers. Both Nb^{5+} (~0.64 Å) and Ti^{4+} (~0.61 Å) have similar ionic radii, allowing Nb^{5+} to easily substitute Ti^{4+} in the TiO_2 lattice [38-40]. Gomes *et al.* [40] reported that the addition of Nb not only reduces the average particle size of TiO_2 but also increased the overall photodegradation efficiency of MB solution up to 44%, compared to 26% for bare TiO_2, due to the excess electrons provided by Nb^{5+}. Furthermore, Kou *et al.* [39] successfully reduced the wide band gap of TiO_2 from 3.1 eV to 2.9 eV through Nb doping, making it more efficient within the visible light range.

On the other hand, boron is a *p*-type dopant that introduces holes into the TiO_2 lattice, creating positive charge carriers. Boron can substitute for oxygen or occupy interstitial sites, effectively inhibiting crystal growth and increasing the total surface area of the photocatalyst. The increased surface area allows more adsorption of pollutant molecules on the catalyst surface, enhancing the degradation efficiency [41-43]. Mulpuri *et al.* [41] reported that the crystallite size of TiO_2 was reduced by almost half upon boron doping, and the band gap of B-TiO_2 was reduced to 2.95 eV compared to 3.12 eV for bare TiO_2. Furthermore, under UV light radiation, the degradation of MB dye by bare TiO_2 was only 28%, whereas B-TiO_2 achieved more than 95% degradation of MB dye, significantly enhancing photocatalytic performance [43]. Nevertheless, a research gap existed where the combined effect of niobium and boron with TiO_2 at different polymorphs has not been explored. Therefore, this research investigates the impact of doping and co-doping TiO_2 with Nb and B at different polymorphs (anatase and rutile) and dopant concentrations (0.25, 0.50, 0.75 and 1.00 mol%) on the photodegradation efficiency of MB dye.

2. Materials and Methods

2.1 Materials

Titanium(IV) isopropoxide (TTIP, CAS #546-68-9, ≥97.0%, Sigma-Aldrich 87560) and ethanol (CAS #64-17-5, 95 v/v% (repack), Chemiz 19546) were used as precursors for synthesizing TiO_2, while hydrochloric acid (HCl, 2M, CAS #7647-01-0, Merck 480934) was used as the initiator for hydrolysis. Niobium powder (Nb, CAS #7440-03-1, Strem 93-4132) and boric acid (H_3BO_3, CAS #10043-35-3, Ajax Finechem 107) were used as dopants. Methylene blue (CAS #61-73-4, BDH Chemical 26132) was used as the dye model to evaluate the photocatalytic performance of the TiO_2-based photocatalyst.

2.2 Synthesis of TiO_2-Based Nanopowders

Pristine, Nb-doped, B-doped, Nb,B-co-doped TiO_2 nanopowders were synthesized using the sol-gel technique, as shown in Figure 1. To synthesize pristine TiO_2, 5.68 mL of TTIP was added dropwise into 40 mL of ethanol under continuous stirring for 30 min to form mixture A. Subsequently, 2 mL of HCl was added dropwise to mixture A under continuous stirring until a gel was obtained. This gel was then dried in an oven at 80 °C for 6 h. The resulting powder was ground in a mortar and calcinated at 400 °C and 900 °C, respectively, at a rate of 3 °C min^{-1} for 2 h.

For Nb-TiO_2, an appropriate amount of niobium powder was dissolved in a mixture of 2 mL of HCl with 10 mL of D.I water to achieve a concentration of 0.5 mol%. This solution was then added to the TTIP and ethanol mixture, and the procedure described above was repeated, as shown in Figure 1. For B-TiO_2, boric acid was dissolved in D.I water without the addition of HCl, and the procedure was repeated. For Nb,B-TiO_2 nanopowders, the Nb precursor solution was added dropwise into the pre-synthesized B-TiO_2 precursor solution under continuous stirring at 80 °C until the entire mixture became gel-like. The heat treatment procedure described above was then repeated.

After selecting the best combination of dopants with TiO_2, the experiment proceeds to the next stage with varying concentrations of dopants (0.25, 0.50, 0.75, 1.00 mol%). The procedures described above were repeated for each concentration.

2.3. Characterizations

The crystalline phase and corresponding crystallite size of all nanopowders were identified using X-ray diffraction (XRD) (Bruker Advanced X-ray D8 Diffractometer) with the Cu Kα radiation (λ=1.5406 Å) at room temperature. The morphology and elemental mapping of the synthesized nanopowders were determined using Ultra-High-Resolution SEM (Hitachi-Regulus 8220). The optical band gap of the synthesized samples was measured using UV-Vis absorption spectra (Varian Cary 50 UV-Vis spectrophotometer) over a wavelength range of 300 – 700 nm and calculated using a Tauc plot.

2.4. Evaluation of Photocatalytic Performances

The photocatalytic performance of all synthesized nanopowders were evaluated by measuring the degradation rates of methylene

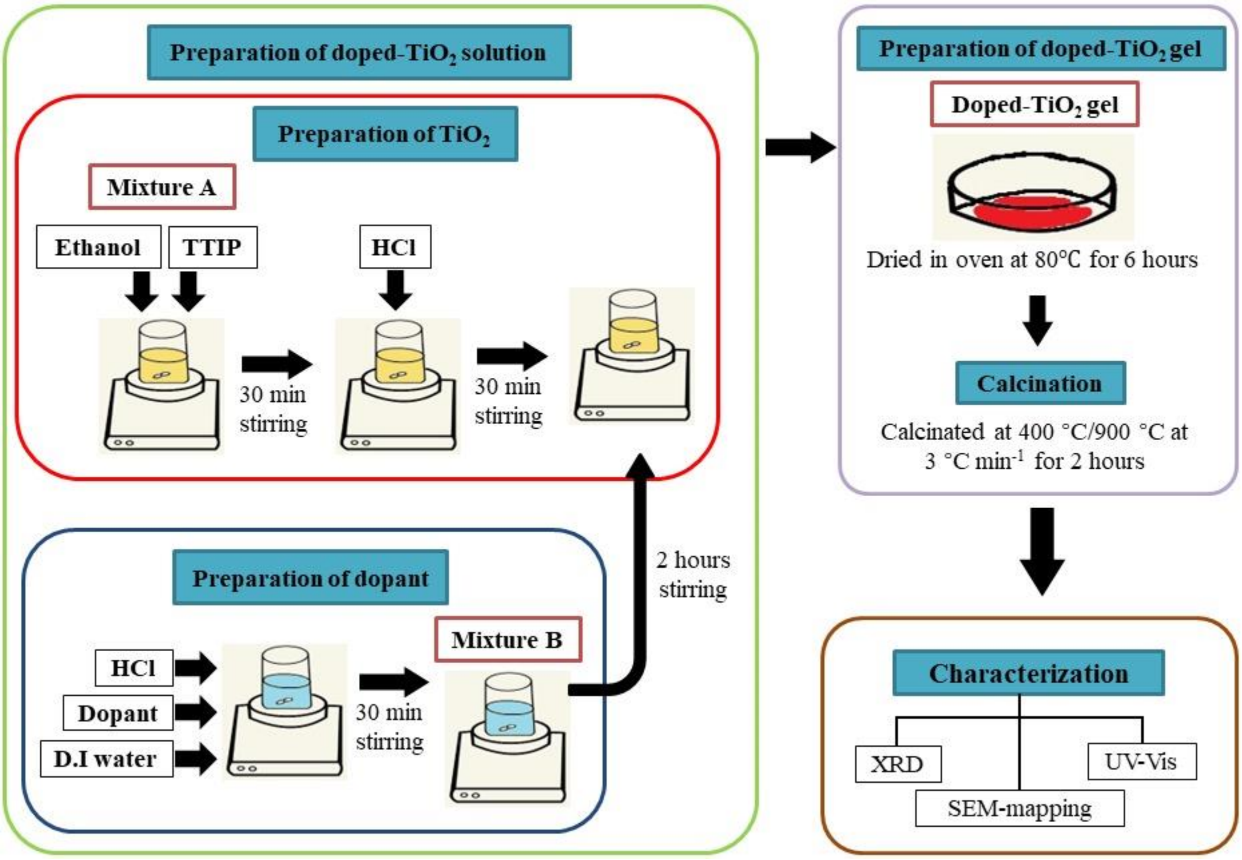

Figure 1. Schematic of the experimental procedure for preparing and characterizing pure, Nb-doped, B-doped and Nb,B-co-doped TiO_2 nanopowders.

blue (MB) solution (2 ppm) under visible light irradiation. 0.02 g of catalyst powder was added to 100 mL of MB dye solution in a glass beaker. The mixture was magnetically stirred in the dark for 30 min to achieve absorption equilibrium [5,44]. Irradiation was then performed using a fluorescent lamp (Philips TLD 18W/865) emitting light in the 400 – 700 nm range, with a peak emission at 550 nm. Samples were analyzed at regular intervals of 30 min for 2 h. The absorption spectra were recorded using a UV-Vis spectrophotometer (Varian Cary 50). The concentration of MB in the solution was determined as a function of irradiation time by monitoring the absorbance change at 664.5 nm, corresponding to the maximum absorption wavelength (λ_{max}) of MB. The removal efficiency of MB dye solution was calculated using Equation (1).

$$R = \frac{C_0 - C_t}{C_0} \times 100\% \qquad (1)$$

where, C_0 is the initial concentration of the MB dye solution and C_t is the concentration of the MB dye solution at the respective time intervals.

3. Results and Discussion

3.1. X-ray Diffraction (XRD) Analyses

The crystal structure of the synthesized samples was characterized using XRD. Figure 2 presents the XRD patterns of all synthesized TiO_2-based nanopowders calcined at 400 °C. The diffraction peaks at 25.37°, 37.9°, 48.16°, 54.0°, 55.20°, 62.87°, 68.98°, 70.48°, 75.28° and 82.93° correspond to the lattice planes (011), (004), (020), (015), (121), (024), (116), (220), (125) and (224), respectively, matching the anatase phase of TiO_2 (ICSD 98-002-4276). Thus, all samples were crystalline and primarily consisted of the tetragonal anatase phase of TiO_2. Additionally, in Nb-TiO_2 and Nb,B-TiO_2 nanopowders, there is an additional peak at 20°, corresponding to Nb_2O_5 (ICDD 00-030-0870). The result suggests that doping niobium into the TiO_2 lattice substituted titanium atoms and bonded with oxygen atoms to form Nb_2O_5 within the lattice. Notably, no additional peaks were observed in B-TiO_2 compared to bare TiO_2, probably due to the amount of boron was too low or had low crystallinity, thus falling below the detection limit of XRD analysis [42,45,46]. However, an additional peak was observed at 31.19° in Nb,B-TiO_2 nanopowders, matching Nb_3BO_9 (ICDD 00-019-0867). This finding suggests that the addition of boron formed bonds with niobium and oxygen atoms, causing interstitial defects within the TiO_2 lattice.

On the other hand, Figure 3 shows the XRD patterns of TiO_2-based nanopowders calcined at 900 °C. The diffraction peaks at 27.45°, 36.09°, 39.21°, 41.26°, 44.07°, 54.35°, 56.66°, 62.78°, 64.09°, 65.55°, 69.05°, 69.83°, 72.46° and 76.57° correspond to the lattice planes of (110), (011), (020), (111), (120), (121), (220), (002), (130), (221), (031), (112), (131), (022), and (122), respectively, which align with the rutile phase of TiO_2 (ICSD 98-008-2086). Thus, all samples were crystalline and primarily consisted of the tetragonal rutile phase of TiO_2. Notably, no additional peaks were observed in the rutile TiO_2-based nanopowders. This finding suggests that the denser tetragonal structure of rutile, with its different arrangement of Ti and O atoms compared to anatase, along with the low amount of dopants, made it more difficult for niobium and boron to be detected in the rutile phase [42,45,46].

However, a minor shift was detected in the (110) lattice plane of rutile TiO_2 toward smaller angles in Nb-TiO_2, B-TiO_2 and Nb,B-TiO_2. Figure 4 (a) and (b) present the comparison of enlarged views of selected angles to highlight the minor shifts in anatase and rutile TiO_2-based nanopowders. The shift in the XRD peaks' position to either higher or lower 2θ suggests the presence

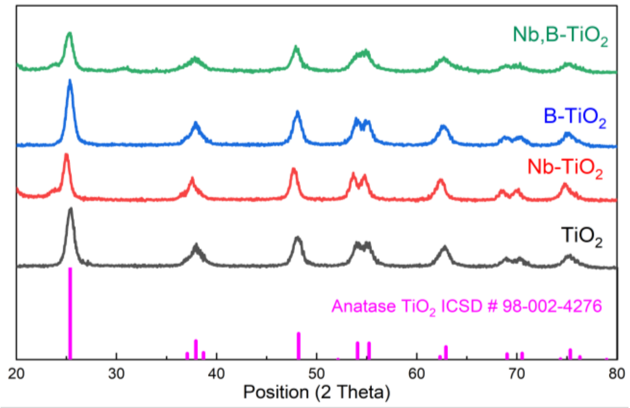

Figure 2. XRD patterns of synthesized TiO_2-based nanopowders calcined at 400 °C.

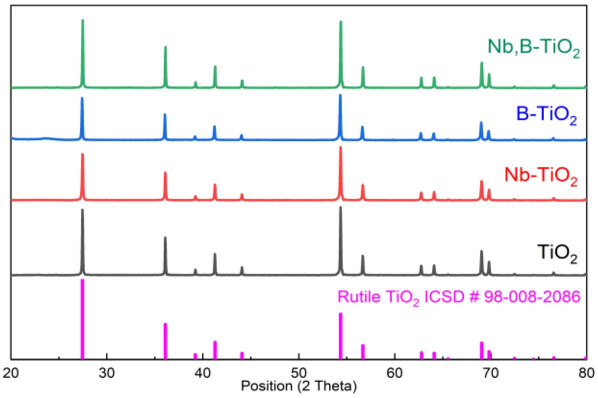

Figure 3. XRD patterns of synthesized TiO_2-based nanopowders calcined at 900 °C.

of lattice distortions or defects due to the strain on the crystal structure [2,35]. This is further supported by comparing the lattice parameters of both anatase and rutile TiO_2-based nanopowders using the formula for the tetragonal system, as shown in Equation (2).

$$\frac{1}{d^2} = \frac{h^2 + k^2}{a^2} - \frac{l^2}{c^2} \tag{2}$$

where, d is the spacing between diffraction planes, θ is the angle of diffraction in radians, λ is the wavelength of X-ray radiation (1.5406 Å), h, k, and l are Miller indices of the lattice plane, and a and c are the lattice parameters for the tetragonal system ($a = b \neq c$). The lattice parameters of the synthesized nanopowders are summarized in Table 1. The change in lattice parameters further supports that niobium and boron were successfully incorporated into the TiO_2 lattice structure, causing the lattice distortion and defects. The role of lattice distortion and defects is related to the observed trend in the photodegradation of methylene blue that will be elaborated in the subsequent paragraphs.

Additionally, the crystallite size (τ) of the synthesized samples was calculated by using Debye-Scherrer's equation [2,35], as shown in Equation (3).

$$\tau = \frac{k\lambda}{\beta \cos\theta} \tag{3}$$

where τ is the crystallite size, k is the Scherrer constant (0.9), λ is the wavelength of X-ray radiation (0.154 nm), and β is the full width at half-maximum intensity. The τ value was determined from the most intense reflection at the (110) peaks of the samples from Figure 4 and summarized in Table 1. From the observations, the crystallite size reduced upon doping process. This was attributed to the presence of lattice distortion and defects caused by the dopants and affecting the grain growth and led to the reduction in crystallite size.

3.2. Scanning Electron Microscopy (SEM) Analyses

Figures 5–12 present the morphological images with elemental mapping of all the

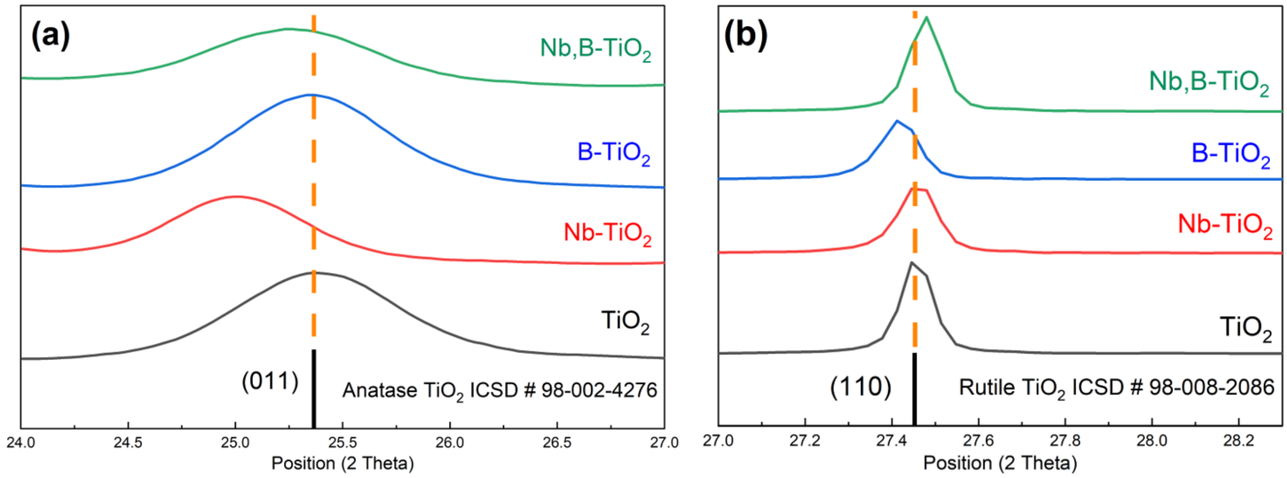

Figure 4. Enlarged views of selected angles to highlight the minor shifts are shown in (a) anatase and (b) rutile TiO_2-based nanopowders, respectively.

Table 1. Summary of physicochemical properties of synthesized TiO_2-based nanopowders.

Calcination Temperature (°C)	Sample	Lattice parameter (Å)		Crystallite size (nm)
		a	c	
400	Anatase TiO_2	3.7843	9.4729	11.0128
	Anatase Nb-TiO_2	3.3800	9.5647	8.8867
	Anatase B-TiO_2	3.7856	9.4831	8.8803
	Anatase Nb,B-TiO_2	3.7971	9.5084	9.1915
900	Rutile TiO_2	4.5902	2.9589	92.3573
	Rutile Nb-TiO_2	4.5899	2.9590	74.2696
	Rutile B-TiO_2	4.5969	2.0937	76.006
	Rutile Nb,B-TiO_2	4.5860	2.9579	89.5192

synthesized TiO_2-based nanopowders, characterized by FESEM. The morphology of the anatase TiO_2-based nanopowders calcinated at 400 °C revealed a quite homogeneous and smaller shape. On the other hand, the morphology of the rutile-based nanopowders calcinated at 900 °C revealed a more irregular and bigger shape compared to anatase. This shows that calcination temperature significantly affected the morphology of the TiO_2-based nanopowders. These results are consistent with the crystallite size calculations from the XRD analyses. The anatase phase typically has a smaller grain size than the rutile phase, as rutile has higher surface energy causing the particles to agglomerate, resulting in larger sizes and smaller specific surface areas [30-32]. Additionally, the average grain size for both anatase and rutile decrease based on the FESEM images with the presence of dopants, which cause lattice distortion and defects. This led to grain-boundary pinning, restricting grain growth, and resulting in smaller grain sizes [47]. The results

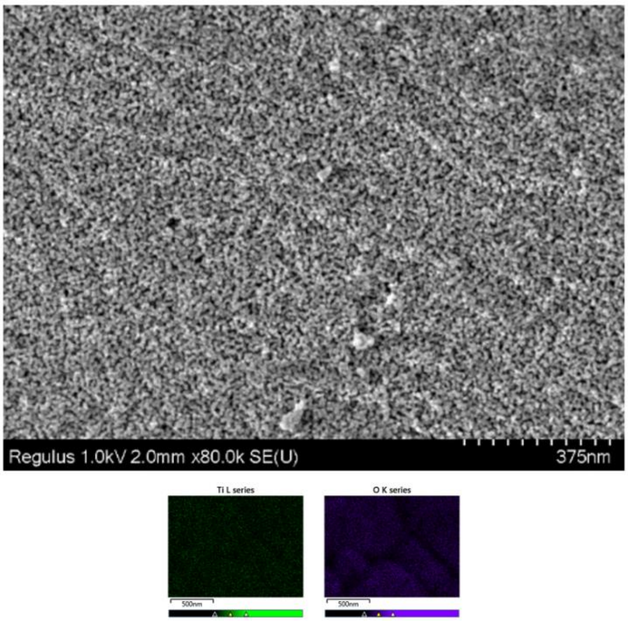

Figure 5. FESEM images of anatase TiO_2 under 80 kX magnification with respective elemental mapping.

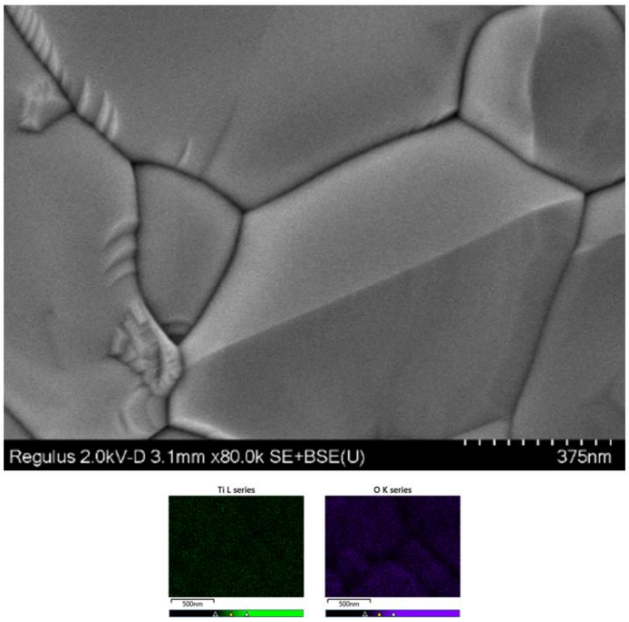

Figure 6. FESEM images of rutile TiO_2 under 80 kX magnification with respective elemental mapping.

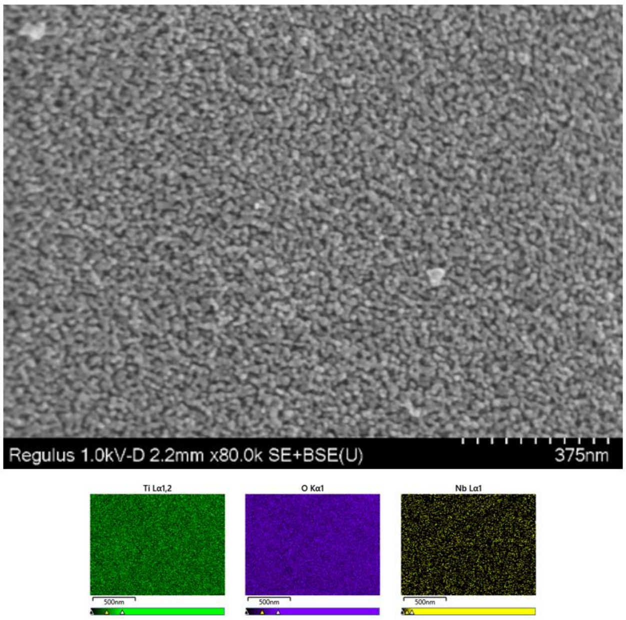

Figure 7. FESEM images of anatase Nb-TiO_2 under 80 kX magnification with respective elemental mapping.

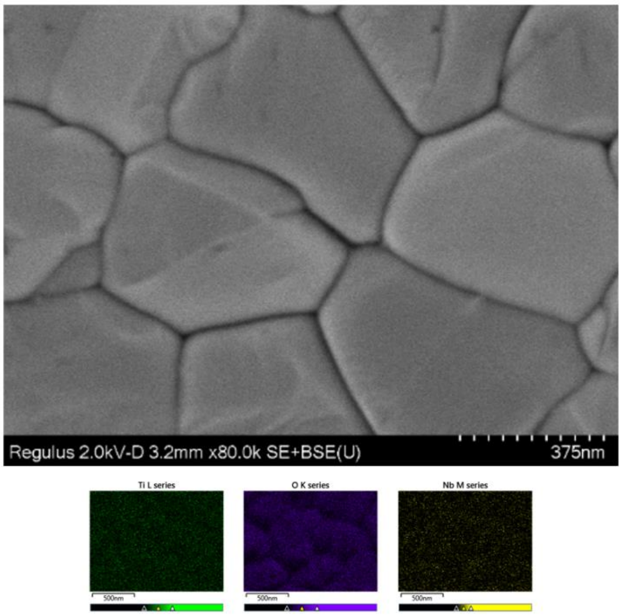

Figure 8. FESEM images of rutile Nb-TiO_2 under 80 kX magnification with respective elemental mapping.

align with the findings from the XRD analyses, supporting the presence of dopants and the resulting distortion within the TiO_2 lattice. The reduction in average grain size is related to the observed trend in the photodegradation of methylene blue, which will be elaborated in subsequent paragraphs. Furthermore, the elemental mapping shows the presence of niobium and boron within the TiO_2, further supporting the XRD data, which could not show the presence of dopants due to its detection limit.

3.3. Photocatalytic Performance of Methylene Blue Using Synthesized TiO_2-based Photocatalyst

Figure 13 and Figure 14 show the UV-Vis absorbance spectra of MB dye solution degraded by all synthesized TiO_2-based nanopowders and compare the removal efficiencies of MB by these nanopowders, respectively. The extent of MB degradation and the photocatalytic performance of the samples over irradiation time were determined by the decrease in the absorbance

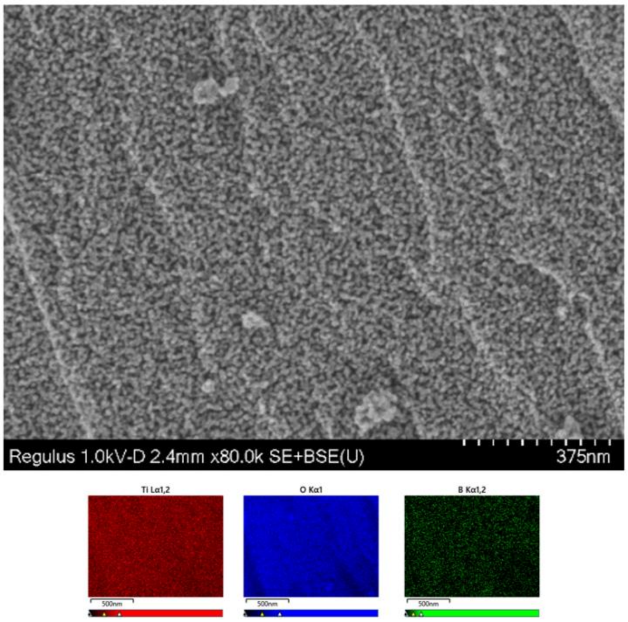

Figure 9. FESEM images of anatase B-TiO_2 under 80 kX magnification with respective elemental mapping

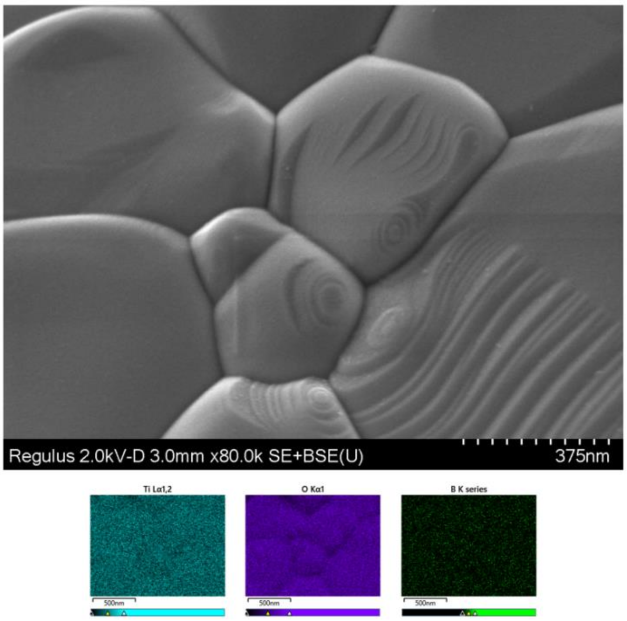

Figure 10. FESEM images of rutile B-TiO_2 under 80 kX magnification with respective elemental mapping

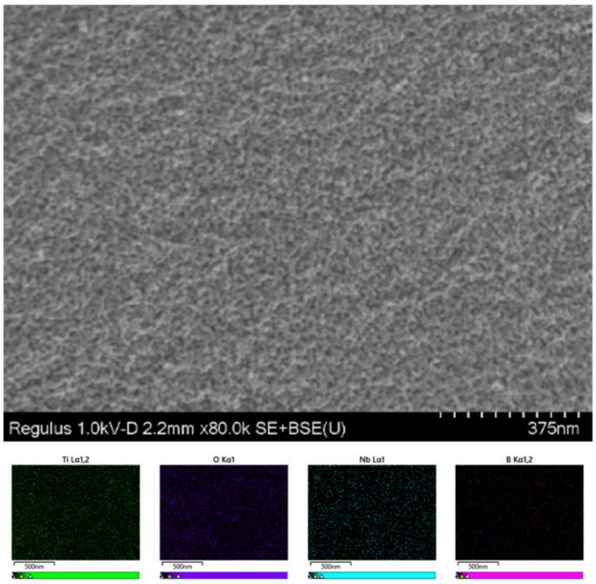

Figure 11. FESEM images of anatase Nb,B-TiO_2 under 80 kX magnification with respective elemental mapping

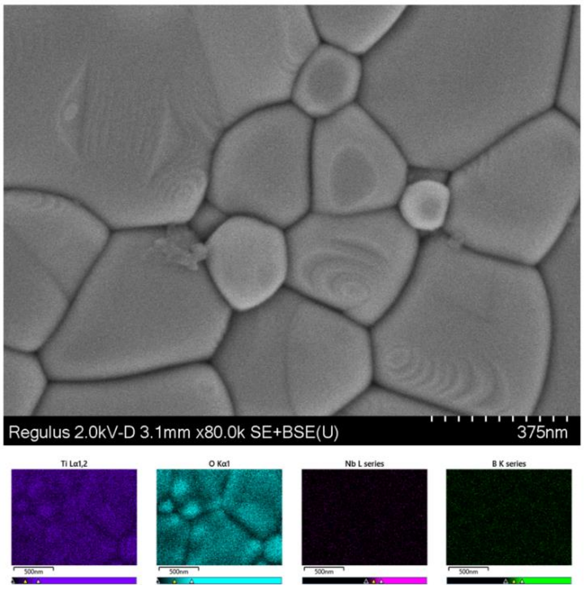

Figure 12. FESEM images of rutile Nb,B-TiO_2 under 80 kX magnification with respective elemental mapping.

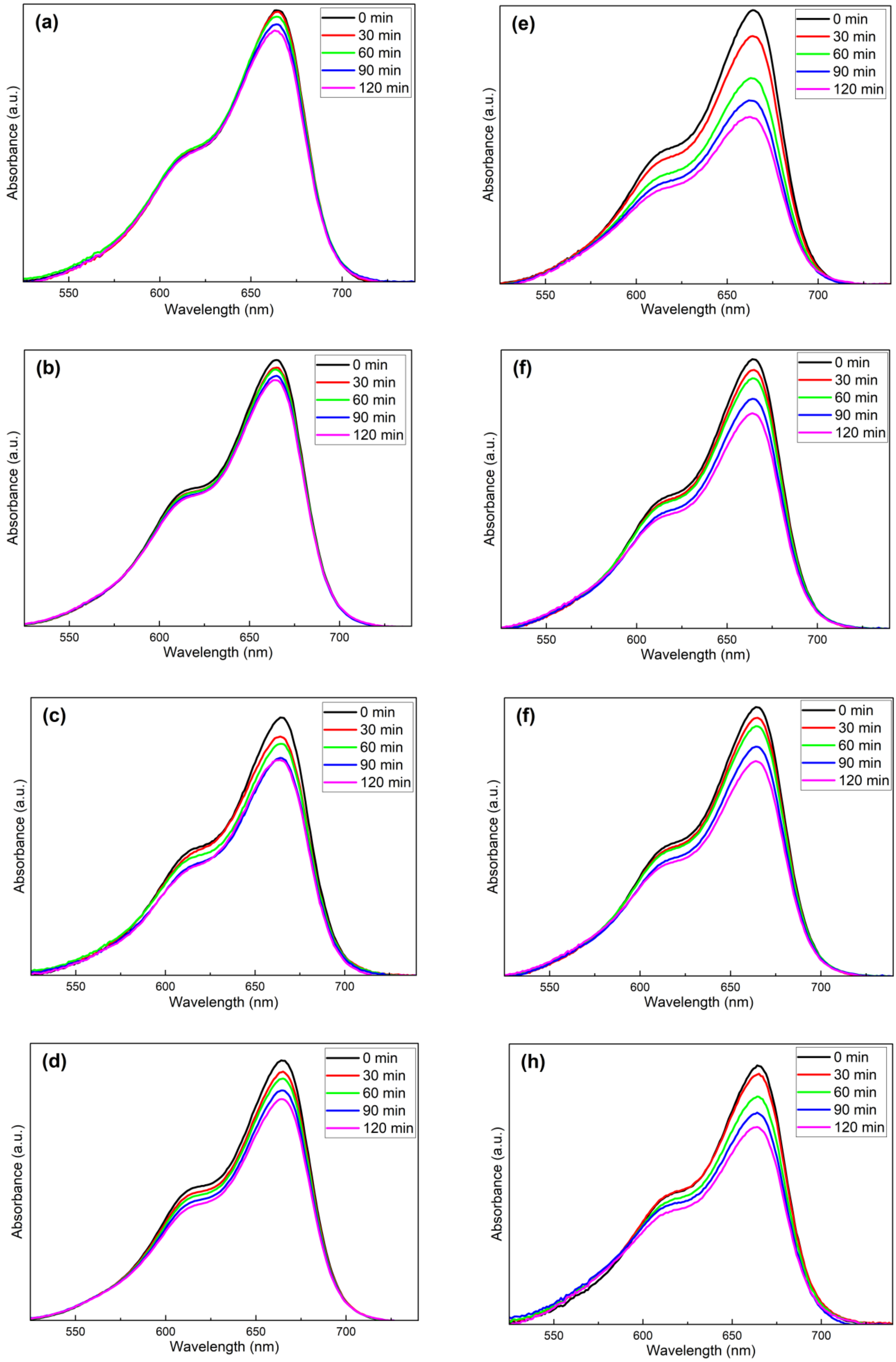

Figure 13. UV-Vis absorbance spectra of MB dye solution degraded by (a) anatase TiO_2, (b) rutile TiO_2, (c) anatase Nb-TiO_2, (d) rutile Nb-TiO_2, (e) anatase B-TiO_2, (f) rutile B-TiO_2, (g) anatase Nb,B-TiO_2 and (h) rutile Nb,B-TiO_2.

value at 664.5 nm, which corresponds to the typical peak in the absorption spectra of MB.

As shown in Figure 13 and Figure 14, anatase typically exhibits higher removal efficiency than rutile for MB dye solution after 120 minutes of visible light irradiation. This finding aligns with the XRD and morphology results, where anatase has a smaller average grain size than rutile, allowing more active sites on the photocatalyst surface to degrade MB dye. Notably, there is minimal difference between the degradation of MB dye by bare anatase TiO_2 (7.97%) and bare

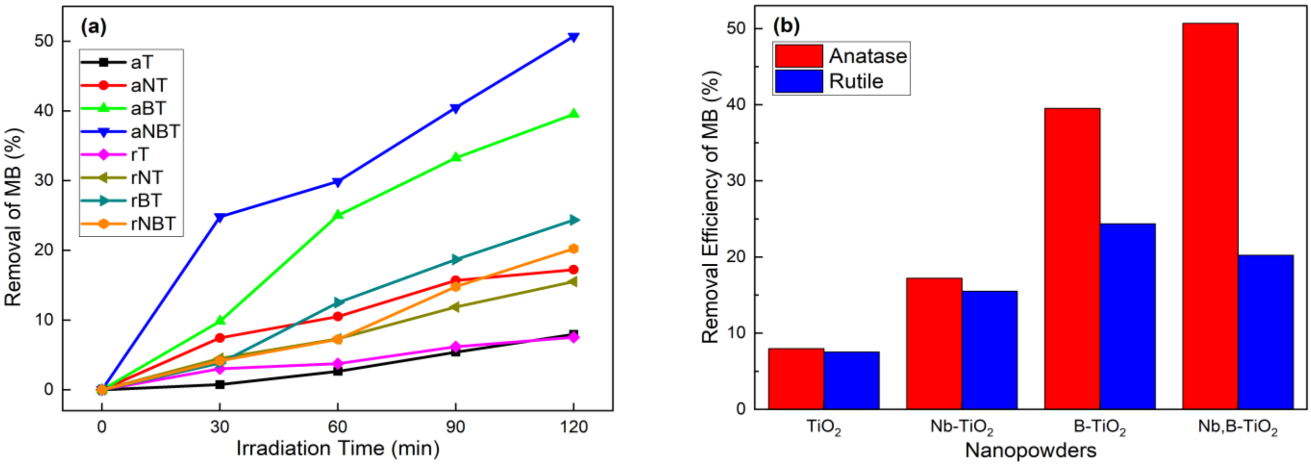

Figure 14. (a) MB removal efficiencies by various synthesized TiO_2-based nanopowders and (b) the respective comparison. aT denotes anatase TiO_2 (black line), aNT denotes anatase Nb-TiO_2 (red line), aBT denotes anatase B-TiO_2 (green line), aNBT denotes anatase Nb,B-TiO_2 (blue line), rT denotes rutile TiO_2 (purple line), rNT denotes rutile Nb-TiO_2 (dark yellow line), rBT denotes rutile B-TiO_2 (dark cyan line), rNBT denotes rutile Nb,B-TiO_2 (orange line).

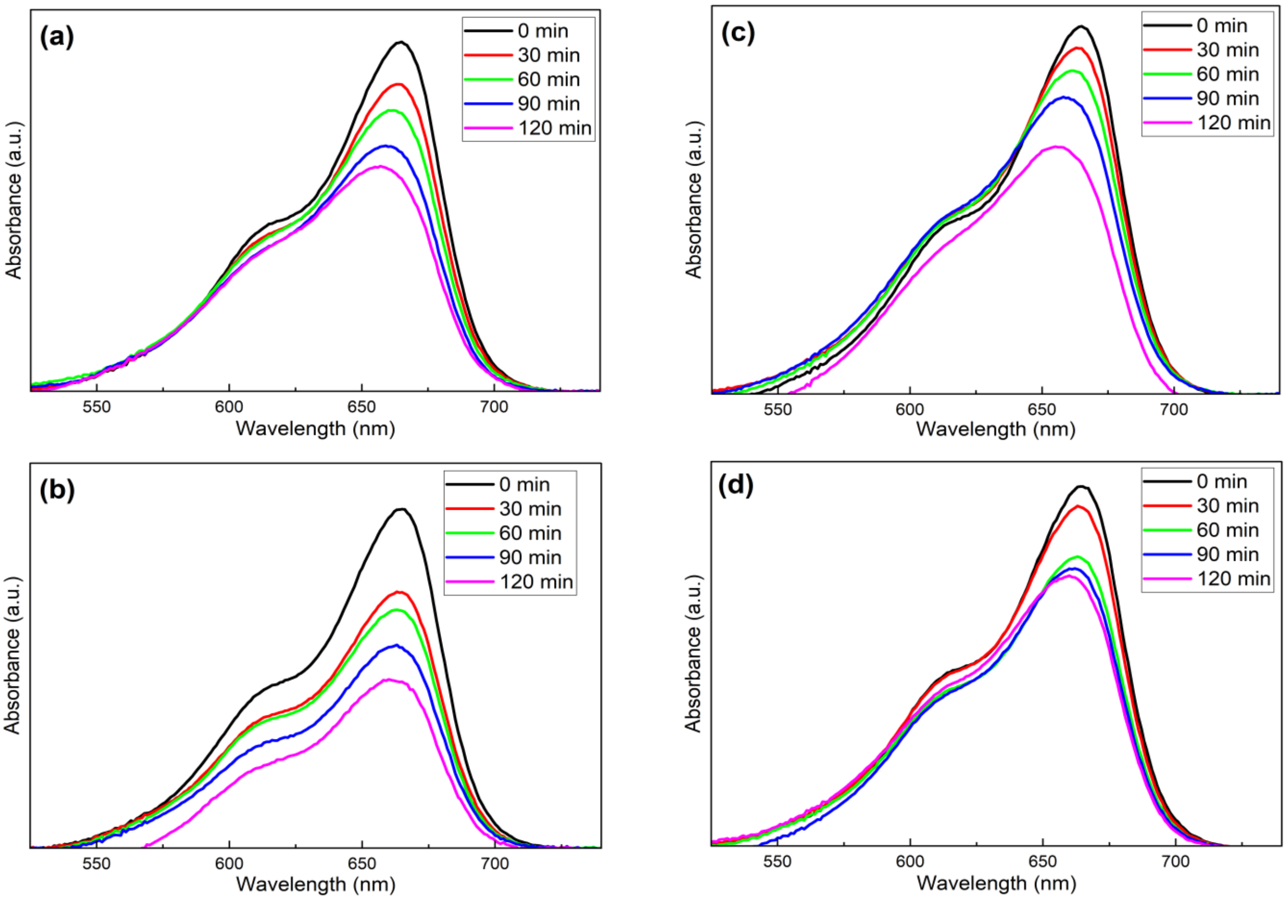

Figure 15. UV-Vis absorbance spectra of MB dye solution degraded by Nb,B-TiO_2 nanopowders with varying concentrations of (a) 0.25 mol%, (b) 0.50 mol%, (c) 0.75 mol%, and (d) 1.00 mol%, respectively.

rutile TiO_2 (7.53%). This suggests that both phases are primarily active under UV light [35-37]. Therefore, the difference in MB dye removal efficiency is minimal, even though anatase has a smaller crystallite size than rutile.

On the other hand, doping process has proven to enhance the photocatalytic performance of bare TiO_2, as shown in Figure 13 and Figure 14. The anatase phase of Nb-TiO_2, B-TiO_2 and Nb,B-TiO_2 shows removal efficiencies of 17.23%, 39.53% and 50.71%, respectively. Conversely, the rutile phase of Nb-TiO_2, B-TiO_2 and Nb,B-TiO_2 shows removal efficiencies of 15.53%, 24.37%, and 20.25%, respectively. The MB removal efficiencies of these doped TiO_2 nanopowders are higher than those of both bare anatase and bare rutile TiO_2. These findings support previous characterization results, where the presence of dopants causes lattice distortion and defects within the TiO_2 lattice, affecting grain growth and leading to a reduction in crystallite size, which allows more active sites on the photocatalyst surface to degrade MB dye. Additionally, it is notable that among the samples, anatase Nb,B-TiO_2 exhibits the highest photocatalytic performance towards MB dye, with a removal efficiency of 49.29%. This indicates that the combination effect of niobium and boron co-doping with anatase TiO_2 is optimal and applicable in wastewater remediation.

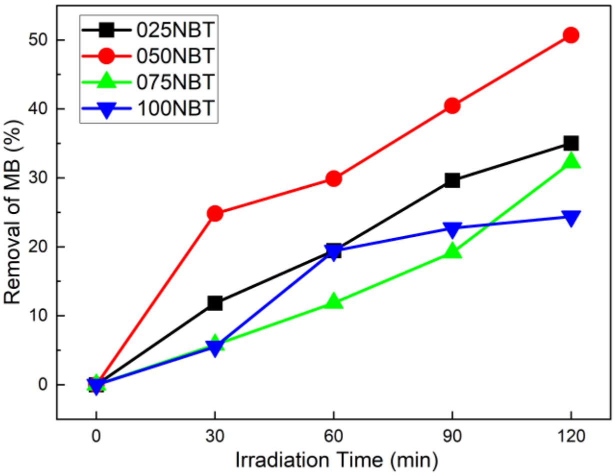

Figure 16. Comparison of MB removal efficiencies by Nb,B-TiO_2 nanopowders with varying dopant concentrations (0.25, 0.50, 0.75 and 1.00 mol%). 025NBT denotes 0.25 mol% Nb,B-TiO_2 (black line), 050NBT denotes 0.50 mol% Nb,B-TiO_2 (red line), 075NBT denotes 0.75 mol% Nb,B-TiO_2 (green line), and 100NBT denotes 1.00 mol% Nb,B-TiO_2 (blue line).

3.4 Photocatalytic Performance of Methylene Blue Using Synthesized Nb,B-TiO_2-based Photocatalyst

The photocatalytic performance of anatase Nb,B-TiO_2 was further investigated by varying the dopant concentrations to 0.25, 0.50, 0.75, and 1.00 mol%. Figure 15 presents the UV-Vis absorbance spectra of MB dye solution degraded by the Nb,B-TiO_2-based nanopowders with varying dopant concentrations, and Figure 16 shows the comparison of MB removal efficiencies for each nanopowders. Table 2 tabulates a comparison of the MB removal efficiencies of the synthesized TiO_2 and Nb,B-TiO_2-based nanopowders. The observed MB removal efficiencies were 35.04%, 50.71%, 32.25%, and 24.41%, for 0.25, 0.50, 0.75, and 1.00 mol% of Nb,B-TiO_2, respectively. Notably, 0.50 mol% Nb,B-TiO_2 exhibited the highest MB removal efficiency among the samples.

These results suggest that incorporating niobium and boron into TiO_2 created Nb^{5+} and B^{3-} defects, which served as more active sites on the photocatalyst surface, thus enhancing the photocatalytic performance. Additionally, it is notable that a low concentration of doping improved the photocatalytic performance, while increasing the dopant concentration causes particle agglomeration [2,48]. In this research, 0.50 mol% of niobium and boron doping into the TiO_2 lattice demonstrated the best photocatalytic degradation towards MB under 120 min of visible light irradiation.

The rate of MB removal by the Nb,B-TiO_2-based nanopowders is further supported by the photodegradation kinetics of MB using the Langmuir-Hinshelwood formula, as shown in Equation (4).

Table 2. Rate constant and band gap energy of the synthesized TiO_2 and Nb,B-TiO_2-based nanopowders.

Samples	Removal efficiency of MB (%)	Rate constant, k ($x10^{-3}$ min^{-1})	Band gap energy, E_g (eV)	Band gap reduction (%)
Anatase TiO_2	7.97	0.714	3.40	-
025NBT	35.04	3.63	2.96	12.94
050NBT	50.71	5.50	2.74	19.41
075NBT	32.25	3.11	3.00	11.76
100NBT	24.41	2.54	3.05	10.29

$$\ln\left(\frac{C_0}{C_t}\right) = kt \qquad (4)$$

where, C_0 is the initial concentration of MB dye solution, C_t is the concentration of dye at time t, and k is the limiting rate constant of the reaction. A graph is plotted between the log of reactant concentration versus time as shown in Figure 17. Linear lines were obtained, indicating that the reaction follows pseudo-first order kinetics. The slope of the lines shows the pseudo-first-order rate constant. Table 2 summarizes the pseudo-first-order rate constant for each Nb,B-TiO_2-based nanopowders. Notably, 0.50 mol% Nb,B-TiO_2 degrades MB at the fastest rate of 0.0055 min^{-1}, supporting the previous MB removal efficiency results among the samples.

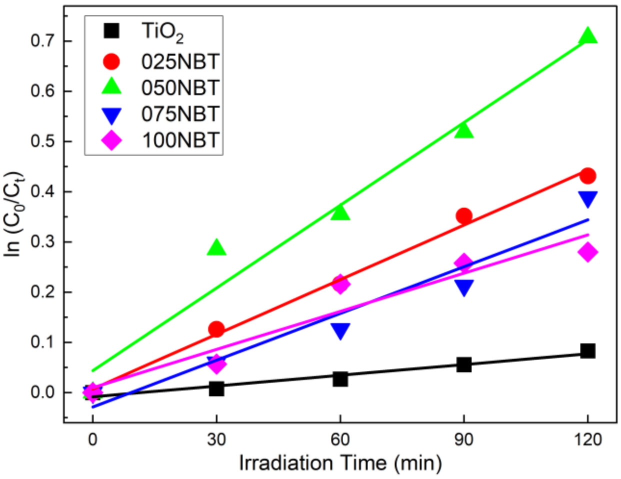

Figure 17. Plot of ln (C_0/C_t) versus time of anatase TiO_2 and Nb,B-TiO_2-based nanopowders. TiO_2 denotes anatase TiO_2 (black line), 025NBT denotes 0.25 mol% Nb,B-TiO_2 (red line), 050NBT denotes 0.50 mol% Nb,B-TiO_2 (green line), 075NBT denotes 0.75 mol% Nb,B-TiO_2 (blue line), and 100NBT denotes 1.00 mol% Nb,B-TiO_2 (purple line).

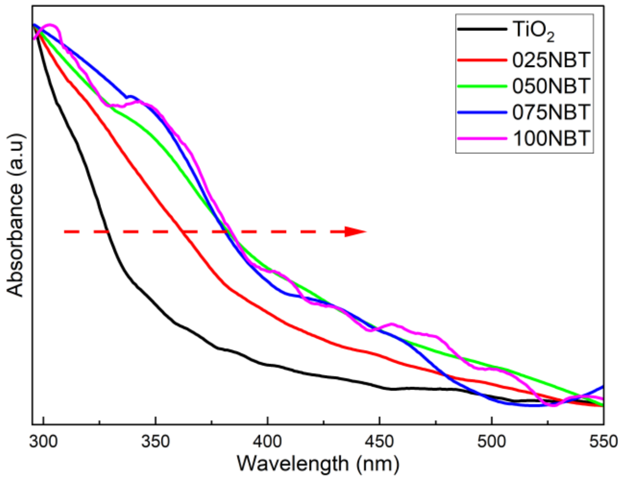

Figure 18. UV-Visible absorbance spectra of anatase TiO_2 and Nb,B-TiO_2-based nanopowders. TiO_2 denotes anatase TiO_2 (black line), 025NBT denotes 0.25 mol% Nb,B-TiO_2 (red line), 050NBT denotes 0.50 mol% Nb,B-TiO_2 (green line), 075NBT denotes 0.75 mol% Nb,B-TiO_2 (blue line), and 100NBT denotes 1.00 mol% Nb,B-TiO_2 (purple line)

3.5 Optical Studies of Synthesized Nb,B-TiO_2-based Photocatalyst

The photocatalytic performance of anatase Nb,B-TiO_2 was further investigated by varying the dopant concentrations to 0.25, 0.50 ,0.75 and 1.00 mol%. The UV-Visible absorbance spectra for anatase TiO_2 and Nb,B-TiO_2-based nanopowders are presented in Figure 18. These absorbance data were then converted into band gap energy *via* the Tauc plot, as described by Equation (5):

$$(\alpha h v)^2 = A(hv - E_g) \qquad (5)$$

where, α is the absorption coefficient, h is the Planck's constant, v is the photon's frequency, A is a proportionality constant, and E_g is the band gap energy. Figure 19 presents the comparison of band gap energies between TiO_2 and Nb,B-TiO_2-based nanopowders *via* the Tauc plot while the band gap energies of the samples are summarized in Table 2.

The results showed that the light absorption of bare anatase TiO_2 was within the UV light range, which is below 400 nm, as shown in Figre 18. Due to its light absorption falls within the UV light range, the bare anatase TiO_2 possessed a wide band gap energy of 3.4 eV, as shown in the Tauc plot Figure 19. These results are consistent with other reported studies [35-37]. However, introducing co-dopants (niobium and boron) into

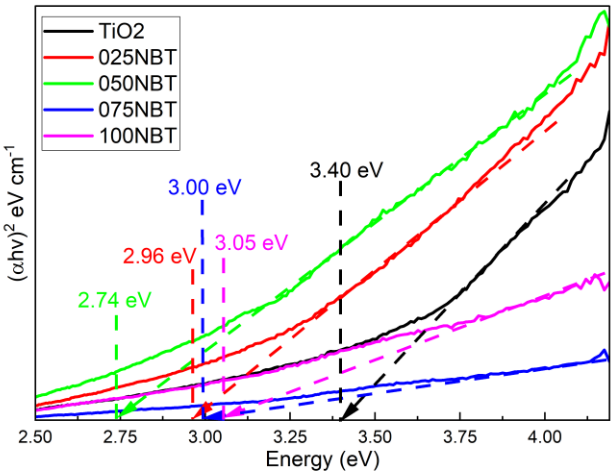

Figure 19. Comparison of band gap energies between bare TiO_2 and Nb,B-TiO_2-based nanopowders.

TiO_2 shifted its light absorption from the UV light range into the visible light range (420 nm and above) as shown in Figure 18. The shift in light absorption results in a reduction of the wide band gap of TiO_2, as shown in Figure 19. The band gap was successfully reduced by up to 12.94%, 19.41%, 11.76% and 10.29%, for 0.25, 0.50, 0.75 and 1.00 mol% of Nb,B-TiO_2, respectively. This reduction was attributed to the synergistic effect of the non-metals, where boron doping lowers the band gap energy of TiO_2, allowing increased absorption of light at extended wavelengths [41-43]. Additionally, niobium acted as an electron trap, effectively preventing the recombination of electron-hole pairs [38,39]. This enhanced charge separation further contributed to a higher photocatalytic performance of Nb,B-TiO_2.

Additionally, it is notable that 0.50 mol% of Nb,B-TiO_2 shows the highest reduction of band gap (19.41%) among the samples, consistent with the previous findings of MB removal efficiency. Beyond this dopant concentartion, the band gap energy increases but remains lower than that of bare TiO_2. These findings align with the previous MB removal efficiency results shown in Figure 16. The increase in band gap energy beyond a specific dopant concentration limit was attributed to the increasing amount of niobium and boron into TiO_2, leading to the particle agglomeration when the dopant concentration beyond a specific limit [2,48]. Therefore, a concentration of 0.50 mol% niobium and boron doping into the TiO_2 lattice demonstrated the best photocatalytic degradation of MB under visible light irradiation.

4. Conclusion

This research successfully synthesized various polymorphs of TiO_2 nanopowders (anatase and rutile), doped with Nb, B, and Nb,B using the sol-gel technique with varying dopant concentrations. Among the samples, the anatase crystal phase of TiO_2 co-doped with 0.50 mol% of niobium and boron demonstrated the highest removal efficiency (50.71%) of MB under 120 min of visible light irradiation. Additionally, the band gap energy of 0.50 mol% Nb,B-TiO_2 nanopowders (2.74 eV) was reduced by 16.41% compared to bare TiO_2 (3.4 eV), significantly enhanced the photocatalytic performance for MB degradation under visible light irradiation. These findings highlight the potential application of the anatase phase of Nb,B-TiO_2, especially at a 0.50 mol% dopant concentration, as a promising visible-light-driven photocatalyst for the removal of organic pollutants and wastewater remediation under visible light in the future.

Acknowledgements

The authors gratefully acknowledge the financial support of the Universiti Sains Malaysia, Special (Matching) Short-Term Grant with Project No: 304.PBAHAN.6315709 and technical support of the School of Materials and Mineral Resources Engineering from Universiti Sains Malaysia.

Credit Authors Statement

Author Contributions: Jia-Zheng Yeoh : Conceptualization, Data curation, Formal analysis, Investigation, Methodology, Roles/Writing - original draft. Phei-Lim Chan: Conceptualization, Data curation, Formal analysis, Investigation, Methodology, Roles/Writing - original draft. Swee-Yong Pung: Conceptualization, Formal analysis, Funding acquisition. Sivakumar Ramakrishnan: Conceptualization, Formal analysis, Investigation, Project administration, Resources, Supervision, Validation, Writing - review & editing. Collin G. Joseph : Validation, Review. Chia-Yun Chen: Validation, Review. All authors have read and agreed to the published version of the manuscript.

References

[1] Pant, B., Park, M., Park, S.J. (2019). Recent advances in TiO_2 films prepared by sol-gel methods for photocatalytic degradation of organic pollutants and antibacterial activities. *Coatings,* 9(10), 613. DOI: 10.3390/coatings9100613.

[2] Paul, R., Kavinarmatha, K., Parthiban, S. (2023). Tantalum doped titanium dioxide nanoparticles for efficient photocatalytic degradation of dyes. *Journal of Molecular Structure*, 1277, 134869. DOI: 10.1016/j.molstruc.2022.134869.

[3] Desch, N., Rheindorf, A., Fassbender, C., Sloot, M., Lake, M. (2023). Photocatalytic degradation of methylene blue by anatase TiO_2 coating. *Applied Research*, in press. DOI: 10.22541/au.169382729.90341592/v2.

[4] Siregar, S.H., Prasetya, P., Norramizawati, N., Marlian, M., Ramadhanti, A.R. (2023). Titanium Dioxide (TiO_2) Modified Bentonite for Photodegradation in Methylene Blue Dye. *Jurnal Kimia Sains dan Aplikasi*, 26(4), 143–150. DOI: 10.14710/jksa.26.4.143-150.

[5] Kerli, S., Kavgacı, M., Soğuksu, A. K., Avar, B. (2022). Photocatalytic Degradation of Methylene Blue, Rhodamine-B, and Malachite Green by Ag@ZnO/TiO_2. *Brazilian Journal of Physics*, 52(1), 22. DOI: 10.1007/s13538-021-01007-1.

[6] Gatou, M.A., Fiorentis, E., Lagopati, N., Pavlatou, E.A. (2023). Photodegradation of Rhodamine B and Phenol Using TiO_2/SiO_2 Composite Nanoparticles: A Comparative Study. *Water*, 15(15), 2773. DOI: 10.3390/w15152773.

[7] Lim, C., An, H.R., Ha, S., Myeong, S., Min, C.G., Chung, H.J., Son, B., Kim, C.Y., Park, J.I., Kim, H., Lee, H.U., Lee, Y.S. (2023). Highly visible-light-responsive nano-porous nitrogen-doped TiO_2 (N-TiO_2) photocatalysts produced by underwater plasma technology for environmental and biomedical applications. *Applied Surface Science*, 638, 158123. DOI: 10.1016/j.apsusc.2023.158123.

[8] Khan, I., Saeed, K., Zekker, I., Zhang, B., Hendi, A. H., Ahmad, A., Ahmad, S., Zada, N., Ahmad, H., Shah, L. A., Shah, T., Khan, I. (2022). Review on Methylene Blue: Its Properties, Uses, Toxicity and Photodegradation. *Water*, 14(2), 242. DOI: 10.3390/w14020242.

[9] Al-Tohamy, R., Ali, S.S., Li, F., Okasha, K.M., Mahmoud, Y.A.G., Elsamahy, T., Jiao, H., Fu, Y., Sun, J. (2022). A critical review on the treatment of dye-containing wastewater: Ecotoxicological and health concerns of textile dyes and possible remediation approaches for environmental safety. *Ecotoxicology and Environmental Safety*, 231, 113160. DOI:10.1016/j.ecoenv.2021.113160.

[10] Manzoor, J., Sharma, M. (2019). Impact of textile dyes on human health and environment. In *Impact of Textile Dyes on Public Health and the Environment*. pp. 162–169. DOI: 10.4018/978-1-7998-0311-9.ch008.

[11] Yardımcı, B., Kanmaz, N. (2023). An effective-green strategy of methylene blue adsorption: Sustainable and low-cost waste cinnamon bark biomass enhanced via MnO_2. *Journal of Environmental Chemical Engineering,* 11(3), 110254. DOI: 10.1016/j.jece.2023.110254.

[12] Oladoye, P.O., Ajiboye, T.O., Omotola, E.O., Oyewola, O.J. (2022). Methylene blue dye: Toxicity and potential elimination technology from wastewater. *Results in Engineering*, 16, 100678. DOI: 10.1016/j.rineng.2022.100678.

[13] Faryad, S., Azhar, U., Tahir, M.B., Ali, W., Arif, M., Sagir, M. (2023). Spinach-derived boron-doped g-C_3N_4/TiO_2 composites for efficient photo-degradation of methylene blue dye. *Chemosphere*, 320, 138002. DOI: 10.1016/j.chemosphere.2023.138002.

[14] Zhong, J., Wen, S., Zhang, L., Wang, J., Liu, C., Yu, J., Zhang, L., Fan, C. (2021). Nitrogen budget at sediment–water interface altered by sediment dredging and settling particles: Benefits and drawbacks in managing eutrophication. *Journal of Hazard Mater*, 406, 124691. DOI: 10.1016/j.jhazmat.2020.124691.

[15] Qian, Y., Chen, Y., Hu, Y., Hanigan, D., Westerhoff, P., An, D. (2021). Formation and control of C- and N-DBPs during disinfection of filter backwash and sedimentation sludge water in drinking water treatment. *Water Research*, 194, 116964. DOI:10.1016/j.watres.2021.116964.

[16] Tang, J., Pu, Y., Zeng, T., Hu, Y., Huang, J., Pan, S., Wang, X.C., Li, Y., Abomohra, A.E.F. (2022). Enhanced methane production coupled with livestock wastewater treatment using anaerobic membrane bioreactor: Performance and membrane filtration properties. *Bioresour Technol*, 345, 126470. DOI: 10.1016/j.biortech.2021.126470.

[17] Cevallos-Mendoza, J., Amorim, C.G., Rodríguez-Díaz, J.M., Montenegro, M.C.B.S.M. (2022). Removal of Contaminants from Water by Membrane Filtration: A Review. *Membranes*, 12(6), 570. DOI: 10.3390/membranes12060570.

[18] Mahto, K.U., Das, S. (2022). Bacterial biofilm and extracellular polymeric substances in the moving bed biofilm reactor for wastewater treatment: A review. *Bioresource Technology*, 345, 126476. DOI: 10.1016/j.biortech.2021.126476.

[19] Li, L., He, Z., Liang, T., Sheng, T., Zhang, F., Wu, D., Ma, F. (2022). Colonization of biofilm in wastewater treatment: A review. *Environmental Pollution,* 93, 118514. DOI: 10.1016/j.envpol.2021.118514.

[20] Waqas, S., Harun, N.Y., Sambudi, N.S., Abioye, K.J., Zeeshan, M.H., Ali, A., Abdulrahman, A., Alkhattabi, L., Alsaadi, A.S. (2023). Effect of Operating Parameters on the Performance of Integrated Fixed-Film Activated Sludge for Wastewater Treatment. *Membranes*, 13(8), 704. DOI: 10.3390/membranes13080704.

[21] Begmatov, S., Dorofeev, A.G., Kadnikov, V.V., Beletsky, A.V., Pimenov, N.V., Ravin, N.V., Mardanov, A.V. (2022). The structure of microbial communities of activated sludge of large-scale wastewater treatment plants in the city of Moscow. *Scientific Reports*, 12(1), 3458. DOI: 10.1038/s41598-022-07132-4.

[22] Ghazal, H., Koumaki, E., Hoslett, J., Malamis, S., Katsou, E., Barcelo, D., Jouhara, H. (2022). Insights into current physical, chemical and hybrid technologies used for the treatment of wastewater contaminated with pharmaceuticals. *Journal of Cleaner Production*, 361, 132079. DOI: 10.1016/j.jclepro.2022.132079.

[23] Saidulu, D., Gupta, B., Gupta, A.K., Ghosal, P.S. (2021). A review on occurrences, eco-toxic effects, and remediation of emerging contaminants from wastewater: Special emphasis on biological treatment-based hybrid systems. *Journal of Environmental Chemical Engineering*, 9(4), 105282. DOI: 10.1016/j.jece.2021.105282.

[24] Nirmala, N., Shriniti, V., Aasresha, K., Arun, J., Gopinath, K.P., Dawn, S.S., Sheeladevi, A., Priyadharsini, P., Birindhadevi, K., Chi, N.T.L., Pugazhendhi, A. (2022). Removal of toxic metals from wastewater environment by graphene-based composites: A review on isotherm and kinetic models, recent trends, challenges and future directions. *Science of the Total Environment*, 840, 156564. DOI: 10.1016/j.scitotenv.2022.156564.

[25] Suhan, M.B.K.M., Al-Mamun, M.R., Farzana, N., Aishee, S.M., Islam, M.S., Marwani, H.M., Hasan, M.M., Asiri, A.M., Rahman, M.M., Islam, A., Awual, M.R. (2023). Sustainable pollutant removal and wastewater remediation using TiO2-based nanocomposites: A critical review. *Nano-Structures and Nano-Objects*, 36, 101050. DOI: 10.1016/j.nanoso.2023.101050.

[26] Thakur, N., Thakur, N., Kumar, A., Thakur, V.K., Kalia, S., Arya, V., Kumar, A., Kumar, S., Kyzas, G.Z. (2024). A critical review on the recent trends of photocatalytic, antibacterial, antioxidant and nanohybrid applications of anatase and rutile TiO2 nanoparticles. *Science of The Total Environment*, 914, 169815. DOI: 10.1016/j.scitotenv.2023.169815.

[27] Navidpour, A.H., Abbasi, S., Li, D., Mojiri, A., Zhou, J.L. (2023). Investigation of Advanced Oxidation Process in the Presence of TiO_2 Semiconductor as Photocatalyst: Property, Principle, Kinetic Analysis, and Photocatalytic Activity. *Catalysts*, 13(2), 232. DOI: 10.3390/catal13020232.

[28] Oruç, P., Turan, N., Cavdar, S., Tuğluoğlu, N., Koralay, H. (2023). Investigation of dielectric properties of amorphous, anatase, and rutile TiO_2 structures. *Journal of Materials Science: Materials in Electronics*, 34(6), 498. DOI: 10.1007/s10854-023-09924-4.

[29] Allen, N.S., Mahdjoub, N., Vishnyakov, V., Kelly, P.J., Kriek, R.J. (2018). The effect of crystalline phase (anatase, brookite and rutile) and size on the photocatalytic activity of calcined polymorphic titanium dioxide (TiO_2). *Polymer Degradation and Stability*, 150, 31–36. DOI: 10.1016/j.polymdegradstab.2018.02.008.

[30] Ghose, K.K., Liu, Y., Frankcombe, T.J. (2023). Comparative first-principles structural and vibrational properties of rutile and anatase TiO_2. *Journal of Physics Condensed Matter*, 35(50), 505702. DOI: 10.1088/1361-648X/acf639.

[31] Kim, M.G., Kang, J.M., Lee, J.E., Kim, K.S., Kim, K.H., Cho, M., Lee, S.G. (2021). Effects of Calcination Temperature on the Phase Composition, Photocatalytic Degradation, and Virucidal Activities of TiO_2 Nanoparticles. *ACS Omega*, 6(16), 10668–10678. DOI: 10.1021/acsomega.1c00043.

[32] Fu, N., Chen, H., Chen, R., Ding, S., Ren, X. (2023). Effect of Calcination Temperature on the Structure, Crystallinity, and Photocatalytic Activity of Core-Shell SiO_2@TiO_2 and Mesoporous Hollow TiO_2 Composites. *Coatings*, 13(5), 852. DOI: 10.3390/coatings13050852.

[33] Eddy, D.R., Permana, M.D., Sakti, L.K., Sheha, G.A.N., Solihudin, G.A.N., Hidayat, S., Takei, T., Kumada, N., Rahayu, I. (2023). Heterophase Polymorph of TiO_2 (Anatase, Rutile, Brookite, TiO_2 (B)) for Efficient Photocatalyst: Fabrication and Activity. *Nanomaterials*, 13(4), 704. DOI: 10.3390/nano13040704.

[34] Holm, A., Hamandi, M., Simonet, F., Jouguet, B., Dappozze, F., Guillard, C. (2019). Impact of rutile and anatase phase on the photocatalytic decomposition of lactic acid. *Applied Catalysis B: Environmental*, 253, 96–104. DOI: 10.1016/j.apcatb.2019.04.042.

[35] Mohamad Idris, N.H., Cheong, K.Y., Smith, S.M., Lee, H.L. (2023). C,N-Co-doped TiO_2 Nanoparticles Immobilized on Floating Alginate Beads for Diazinon Removal under Solar Light Irradiation. *ACS Applied Nano Materials*, in press. DOI: 10.1021/acsanm.3c03622.

[36] Al-Mamun, M. R., Kader, S., Islam, M. S. (2021). Solar-TiO_2 immobilized photocatalytic reactors performance assessment in the degradation of methyl orange dye in aqueous solution. *Environmental Nanotechnology, Monitoring and Management*, 16, 100514. DOI: 10.1016/j.enmm.2021.100514.

[37] Kader, S., Al-Mamun, M.R., Suhan, M.B.K., Shuchi, S.B., Islam, M.S. (2022). Enhanced photodegradation of methyl orange dye under UV irradiation using MoO_3 and Ag doped TiO_2 photocatalysts. *Environmental Technology and Innovation*, 27, 102476. DOI: 10.1016/j.eti.2022.102476.

[38] Wu, M.C., Lin, T.H., Chih, J.S., Hsiao, K.C., Wu, P.Y. (2017). Niobium doping induced morphological changes and enhanced photocatalytic performance of anatase TiO_2. *Japanese Journal of Applied Physics*, 56(4), 04CP07. DOI: 10.7567/JJAP.56.04CP07.

[39] Kou, Y., Yang, J., Li, B., Fu, S. (2015). Solar photocatalytic activities of porous Nb-doped TiO_2 microspheres by coupling with tungsten oxide. *Materials Research Bulletin*, 63, 105–111. DOI: 10.1016/j.materresbull.2014.11.050.

[40] Gomes, G.H.M., de Jesus, M.A.M.L., Ferlauto, A.S., Viana, M.M., Mohallem, N.D.S. (2021). Characterization and application of niobium-doped titanium dioxide thin films prepared by sol–gel process. *Applied Physics A: Materials Science and Processing*, 127(8), 641. DOI: 10.1007/s00339-021-04781-6.

[41] Mulpuri, R.K., Tirukkovalluri, S.R., Imandi, M.R., Alim, S.A., Kapuganti, V.D.L. (2019). Zinc and boron co-doped nano titania with enhanced photocatalytic degradation of acid red 6A under visible light irradiation. *Sustainable Environment Research*, 1(1), 29. DOI: 10.1186/s42834-019-0031-6.

[42] Cano-Casanova, L., Ansón-Casaos, A., Hernández-Ferrer, J., Benito, A.M., Maser, W.K., Garro, N., Lillo-Ródenas, M.A., Román-Martínez, M.C (2022). Surface-Enriched Boron-Doped TiO_2 Nanoparticles as Photocatalysts for Propene Oxidation. *ACS Applied Nano Materials*, 5(9), 12527–12539. DOI: 10.1021/acsanm.2c02217.

[43] Moreira, A J., Dos Santos, B.R.M., Dias, J.A., Rabello, P.T., Coelho, D., Mascaro, L.H., Freschi, G.P.G., Gobato, Y.G., Galeti, H.V.A., Mastelaro, V.R., Pereira, E.C. (2023). Photoactivity of boron- or nitrogen-modified TiO_2 for organic pollutants degradation: Unveiling the photocatalytic mechanisms and by-products. *Journal of Environmental Chemical Engineering*, 11(1), 109207. DOI: 10.1016/j.jece.2022.109207.

[44] Muneeb, A., Rafique, M.S., Murtaza, M.G., Arshad, T., Shahadat, I., Rafique, M., Nazir, A. (2023). Fabrication of Ag–TiO_2 nanocomposite employing dielectric barrier discharge plasma for photodegradation of methylene blue," *Physica B: Condensed Matter*, 665, 414995. DOI: 10.1016/j.physb.2023.414995.

[45] Wu, Y., Gong, Y., Liu, J., Zhang, Z., Xu, Y., Ren, H., Li, C., Niu, L. (2017). B and Y co-doped TiO_2 photocatalyst with enhanced photodegradation efficiency. *Journal of Alloys and Compounds*, 695, 1462–1469. DOI: 10.1016/j.jallcom.2016.10.284.

[46] Ren, Y., Zhao, L., Zou, Y., Song, L., Dong, N., Wang, J. (2019). Effects of different TiO_2 particle sizes on the microstructure and optical limiting properties of TiO_2/reduced graphene oxide nanocomposites. *Nanomaterials*, 9(5), 730. DOI: 10.3390/nano9050730.

[47] Mogal, S.I., Gandhi, V.G., Mishra, M., Tripathi, S., Shripathi, T., Joshi, P.A., Shah, D.O. (2014). Single-step synthesis of silver-doped titanium dioxide: Influence of silver on structural, textural, and photocatalytic properties. *Industrial and Engineering Chemistry Research*, 53(14), 5749–5758. DOI: 10.1021/ie404230q.

[48] Mohtar, S.S., Aziz, F., Ismail, A.F, Sambudi, N.S., Abdullah, H., Rosli, A.N., Ohtani, B. (2021). Impact of Doping and Additive Applications on Photocatalyst Textural Properties in Removing Organic Pollutants: A Review. *Catalysts*, 11(10), 1160. DOI: 10.3390/catal11101160.